sciendo

Polish Journal of Chemical Technology, 26, 4, 8—16, 10.2478/pjct-2024-0034

Effect of metal addition of Cu, Ni, and Fe on swelling Zeolit Alam Lampung (ZAL) to present amphoteric features on Cu-Ni-Fe/ZAL swelling

Prahady Susmanto[1, 2], Ambo Intang[1], Muhammad Djoni Bustan[1, 2*], Sri Haryati[1, 2]

[1]Department of Doctoral Engineering, Faculty of Engineering, Sriwijaya University, Ogan Ilir 30862, Indonesia
[2]Department of Chemical Engineering, Faculty of Engineering, Sriwijaya University, Ogan Ilir 30862, Indonesia
[*]*Corresponding author:* e-mail: muhammaddjonibustan@ft.unsri.ac.id

The main challenge in using Zeolit Alam Lampung (ZAL) as a catalyst lies in controlling its acidic nature which is influenced by the content of alkali metals, alkaline earth metals, transition metals, and Si/Al ratio. Controlling by reducing and adding metals with higher acidity is necessary. This research involved two stages: ZAL Swelling formation followed by adding Cu, Ni, and Fe metals to make a Cu-Ni-Fe/ZAL Swelling catalyst. The acid distribution analysis using the NH_3-TPD profile test showed that the Cu-Ni-Fe/ZAL swelling catalyst exhibited higher Lewis-type acidity and more uniform distribution compared to Brønsted acid. The addition of Cu, Ni, and Fe metals can modify the acidity strength of ZAL Swelling to form Cu-Ni-Fe/ZAL Swelling catalysts with Lewis and Brønsted sites at lower temperatures (120–550 °C) compared to ZAL Swelling (120–750 °C). This gives an idea about the optimization of the arrangement of Lewis and Bronsted acid sites to present amphoteric features.

Keywords: Zeolit Alam Lampung; Natural Zeolite; Bronsted and Lewis Acid; Amphoteric Features.

INTRODUCTION

Indonesia is one of the countries that has diversity and is rich in mining materials, especially natural zeolite. Natural zeolite is one of the mined materials with various physical properties, including thermal stability, high porosity, ion exchange capability, and regular crystal structure[12]. The natural potential of natural zeolite is the concern of the Indonesian government and foreign businesses to develop investment in this natural resource sector. Some natural zeolite-producing areas are Sumatra (Lampung, North Sumatra), Java (West Java, Central Java, East Java), East Nusa Tenggara, and Sulawesi[3]. Lampung Natural Zeolite (ZAL) is a natural zeolite that has a crystal structure of *clinoptilatite*[4]. According to data from the Directorate of Regional Potential Development in 2012, the potential of zeolite natural resources in the province of Lampung Indonesia amounted to 31,173,505 tons[5].

Natural zeolite is one of the natural materials widely used as catalysts, which depends on the number or distribution of catalyst-active sites possessed by natural zeolites[6, 7]. Utilizing zeolite as a catalyst cannot be separated from the role of alumina (Al) and silica (Si), the main constituent compounds. Al^{3+} and Si^{4+} compounds in a natural zeolite framework are anions, while alkali and alkaline earth metals (Na, Mg, K, Ca), as well as Fe and Cu transition metals are variable cations in natural zeolite structures[8]. Indonesia is one of the countries with natural zeolite resources, one of which is Zeolit Alam Lampung (ZAL).

As a catalyst, the zeolite active site is strongly influenced by the acidic functional groups, both Bronsted and Lewis[9], so the success of zeolites as catalysts can not be separated from the combination of the two acids[10]. The active acid site center of zeolite is strongly influenced by the number of Si and Al atoms and the influence of alkali and alkaline earth metal cations in the natural zeolite. Several methods are used to modify natural zeolites as catalysts to increase the active site, among others, by dealumination and alkali treatment, which can regulate the amount of Lewis/Broensted acid sites[11–13].

Acidic properties are chemical properties that must be considered in developing natural zeolites as catalysts. The reaction conversion, the yield of the desired product, the life of the catalyst, and the ease of regeneration are highly dependent on the acidity value or Determination of The Acidity Value (Pka) of the catalyst[14]. The Pka value is greatly influenced by how acid sites are spread out. Consequently, the acidity of the zeolite is intricately linked to both its crystal structure and its chemical composition, specifically regarding the presence of metals and metal compounds. One of the active acid sites of particular concern is the distribution of Al subsumed into Si sites, where the Si/Al ratio will influence the charge balance of cations and heteroatoms[13].

The process of preparation and control of acid sites is an essential part of preparing ZAL as a catalyst, and this cannot be separated from the intrinsic acidity in ZAL linked to Brønsted acid sites. The hydroxyl group Si-O (H)-Al is formed from protons directly bound to O atoms, connecting Al atoms and Si atoms on each side, resulting in the structure of Brønsted acid sites[15]. Lewis acid sites are formed due to the presence of the Al(OH)Si bridge in Si-O− (H+)-Al− or resonance form SiOH→Al (Derouane et al., 2013). Substituting alkali and alkaline earth metals with metals that are more basic in naturally occurring zeolites can alter or regulate Lewis acidity. This cannot be separated from changes in the electrophilicity index, which changes the characteristics of the zeolite[16, 17]. Adding alkali metals or alkaline soils increases zeolite's acidity value, where this event encourages the formation of Lewis acidic sites[18].

The addition or reduction of metal in both natural and synthesized zeolites affects the properties of Brønsted and Lewis acid sites. Adding Fe, Cu, and Co metals to ZSM-5 zeolite by impregnation method resulted in a significant decrease in Brønsted acid sites, but the number Lewis acid sites increased[19]. The addition of Zr^{4+} on zeolite Y increased the density of strong Brønsted acidity by 244.7% from previously only 0.085 mmol/gr. In addition to increasing Brønsted acidity, adding Ni10%/YBCZ heteroatoms increased Lewis acid sites

on zeolite Y from a Brønsted to Lewis (B/L) ratio of 7.6 to 5[20]. One method that can be used to produce an amphoteric catalyst is by combining Lewis and Brønsted acids. Mixing metal chlorides like $FeCl_3$, $CrCl_3$, $ZnCl_2$, and $CuCl_2$, which act as Lewis acids, with Brønsted acid compounds such as H_2SO_4, H_3PO_4, and HCl will increase H+ ions[21]. Phosphate group compounds which are Brønsted acid sites combined with TiO_2 (Lewis acid sites) are bifunctional catalysts that can control the course of the reaction[22].

Incorporation of heteroatoms in zeolite frameworks is a method to modify surface acidity, pore structures, and particle size. The commonly used zeolite heteroatom synthesis method to regulate Lewis acid sites and Brønsted acid sites is currently by isomorphous substitution[23–25].

Replacement or reduction of alkali or alkaline earth metals in natural zeolites, in addition to changing the structure of Brønsted acid sites or Lewis acid sites, also influences thermal stability and pore structure. In addition to affecting the distribution of active sites, silica (Si) and alumina (Al) content also affect the thermal stability of the zeolite. Zeolites with a high Si content will have high thermal stability, while an increase in Al content will decrease thermal stability[14]. The process of reducing alkali, alkaline earth, and transition metals in natural zeolites does not rule out the possibility of producing an extra-large pore due to ealumination and desilication that occurs[26].

The addition of metal not only affects the acidity properties of a catalyst but also influences the course of the reaction, leading to the products that will be produced from a catalyst. Ni, Zn, Cu, and Al metals in pyrolysis of biomass result in an increase in gas products, Al which affects the Lewis acid, Cu, which is more weakly acidic, tends to produce coke products, while Zn and Ni which are more Brønsted acid produce monocyclic aromatic hydrocarbons[27].

This research aims to analyze changes in functional group characteristics, morphology, pore diameter, Thermal Gravimetric Analysis, and acid distribution profile of ZAL into a Cu-Ni-Fe/ZAL amphoteric Swelling catalyst. Developing an amphoteric catalyst is inseparable from the complexity of a reaction on a big aromatics hydrocarbon that requires a catalyst that can regulate the reaction product at low temperatures. Regulation of heteroatom content and pore structure on ZAL is also a concern in developing Lewis acid and Brønsted acid sites. In this study, the amphoteric properties of ZAL were obtained by reducing more basic alkali and alkaline earth metals to produce Swelling ZAL, followed by the addition of more acidic Cu, Ni, and Fe metals to generate Swelling ZAL structures with a combination of more evenly distributed Lewis acid and Brønsted acid sites, while maintaining the crystalline quality of Cu-Ni-Fe/ZAL Swelling. This research will observe the changes in functional groups, crystal structure, the distribution of Cu Ni and Fe metals, the surface area formed, the thermal stability, and the acid distribution profile of the Cu-Ni-Fe/ZAL Swelling catalyst.

MATERIALS AND METHODS

Materials

The natural zeolite is Zeolit Alam Lampung (ZAL) from Bratachem Sub Branch Palembang, $Cu(NO_3)_2 \cdot H_2O$, $Ni(NO_3)_2 \cdot 6H_2O$ 50 and $Fe(NO_3)_3 \cdot 9H_2O$ from Merck Indonesia.

Preparation of ZAL Swelling

The manufacture of ZAL swelling starts with ZAL 100 gr 100 mesh mixed with $C_{15}H_{32}$ in a ratio of 1:10, which is then stirred using a magnetic stirrer at 2500 rpm with a temperature of 80 °C for 30 minutes. Then, the filtration stage was continued, and the mixture dried in the oven for 12 hours at 150 °C.

Preparation of Cu-Ni-Fe/ZAL Swelling Catalyst

10 grams of ZAL Swelling was mixed with 50 grams of $Cu(NO_3)_2 \cdot 3H_2O$, 20 grams of $Ni(NO_3)_2$. $6H_2O$, and 50 grams of $Fe(NO_3)_3 \cdot 9H_2O$ to achieve a mixture pH of 2.5. Furthermore, stirring was carried out using a magnetic stirrer at 2500 rpm for 5 hours, followed by filtration and drying at 150 °C for 12 hours. Calcination was carried out at a temperature of 300 °C for 3 hours to obtain the structure and increase the effectiveness of the catalyst.

Characterization of Catalyst

Functional cluster structure analysis using Fourier Transform Infra-Red (FTIR) Nocole iS10 Non-ATR, X-Ray Diffraction (XRD) analysis using X-Ray Diffraction SHIMADZU XRD-7000, the sample was placed at Cu-Kα 30kV 10mA with a scan speed of 10.0 deg/min, 2θ range 4°–90°. SEM EDX morphology analysis, and Mapping using JSM-6510 Series Scanning Electron Microscope – JEOL Ltd, with an enlargement of 5000 x 5 μm.

Morphological analysis and elemental analysis were performed by Scanning Electron Microscopy (SEM) with field emission and Energy-dispersive X-ray Spectroscopy (EDX), (JED-2300, JEOL), operating at 20 kV with various magnifications were used to observe the surface morphology and element distribution Brunauer-Emmett-Teller (BET) analysis was performed using Quantachrome® ASiQwin™ – Automated Gas Sorption Data Acquisition and Reduction, using Nitrogen gas (N_2). The out gas time was 3 hours and the out gas temperature was 300 °C.

Thermal Gravimetric Analysis (TGA) and Differential Thermal Analysis (DTA) analysis using SIMULTANEOUS TG-DTA (Hitachi brand, STA-200RV). samples were heated up from room temperature to 550 °C at a rate of 20 °C min^{-1}in a flow (100 cm^3 min^{-1}) of nitrogen. The mass loss in the TG curve (30–500 °C) was chosen for the conversion factor calculations, as it is this stage that is connected with desorption of surface-adsorbed water, and removal of water molecules from the channels/void system of the sample structure.

Temperature-programmed desorption of ammonia (NH_3-TPD) analysis using Micromeritics Chemisorb 2750. This analysis aims to measure the acid distribution profile of the sample. Where at the retreat stage the sample is heated at 350 °C for 60 min in He gas con-

ditions (inert). Followed by the NH_3 Adsorption stage (5% in He, v/v) carried out at a temperature of 100 °C for 30 minutes, then imurged with He gas (inert) at the same temperature, for 30 minutes. NH3 desorption is performed at 100–800 °C with a temperature raising rate of 10 °C/min.

RESULTS AND DISCUSSION

FTIR Analysis

The FT-IR spectra of ZAL and ZAL Swelling in Fig. 1 (a) and Fig. 1 (b) show a significant decrease in the % transmittance of ZAL Swelling, indicating an overall increase in the content of Si and Al atoms, in addition to a decrease in the content or concentration of alkali and alkali earth metals and transition metals (T) bound to Si and Al groups. This condition is evidenced by the decrease in the % transmittance intensity of ZAL Swelling compared to ZAL in the range of 400–400 cm^{-1} and 680–850 cm^{-1} which respectively shows the presence of low vibrations in Si-O-T, Al-O-T, and the presence of open pores in O-Si-O and O-Al-O which is marked by a peak shift from 792.72 cm^{-1} in ZAL to 748.87 cm^{-1} in ZAL Swelling[28–31]. The hydroxyl group, in the range of 1499–1617 cm^{-1} and 3000–3800 cm^{-1}, shows a decrease

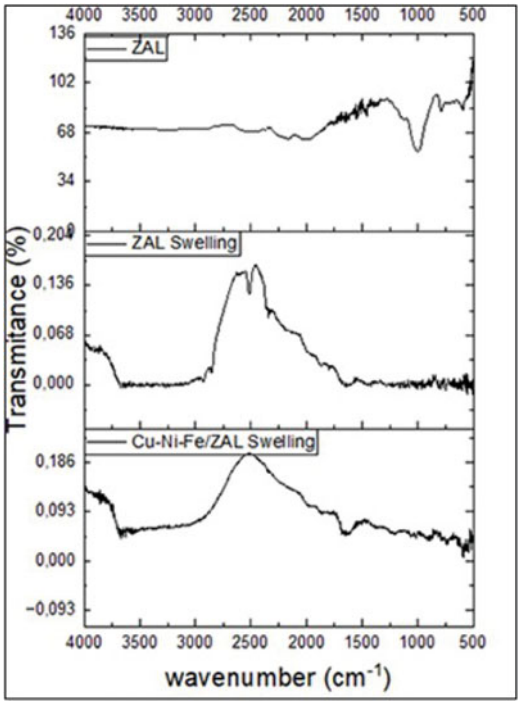

Figure 1. FT-IR Spectra Profile; (a) ZAL; (b) ZAL Swelling; (c) Cu-Ni-Fe/ZAL Swelling Catalysts

in %transmittance of O-H-T (metal) by 70% in ZAL Swelling compared to ZAL[31–33].

Figure 1(b) and Fig. 1(c) show the FTIR spectra formed by ZAL Swelling and encapsulated Cu-Ni-Fe metal (T) on zeolite swelling (Cu-Ni-Fe/zeolite swelling). Encapsulated is characterized by changes in zeolite framework bonds, where there is a 50% change in % transmittance in Si-O-T and Al-O-T bonds in the 400–500 cm^{-1} range. In the range of 680–850 $cm^{-1,}$ there is a change in the % transmittance of symmetric O-Si-T or O-Al-T by 40% and a peak shift from 795.78 cm^{-1} in ZAL Swelling to 738.98 cm^{-1} in (Cu-Ni-Fe/ZAL Swelling). Asymmetric O-Si-T and O-Al- T peak shifts from the previous 1007 cm^{-1} shifted to 906.36 cm^{-1} [34]. In addition, there is also a change in % transmittance in the asymmetric O-Si-T and O-Al-T groups by 40% compared to ZAL Swelling. Si-OH and Al-OH structures do not show a shift, and the peak indicates this at 1651.75 cm^{-1}. At 2500 cm^{-1}, deformation of the water molecule structure occurs. From the results of this FTIR spectra analysis, Cu-Ni-Fe/ZAL Swelling shows a change in the framework-bond, especially in the structure of Si-O-T, Al-O-T, O-Si-T, O-Al-T which shows Cu, Ni and Fe metals are bound to the structure. The Si-OH (cyanol) and Al-OH clusters in the 1600–1700 cm^{-1} range do not show changes in framework bonds.

XRD Analysis

Figure 2 shows XRD diffraction patterns of crystalline ZAL, ZAL Swelling, and Cu-Ni-Fe/ZAL Swelling. XRD results of ZAL and ZAL Swelling show a decrease in the quality of crystals and crystal damage characterized by a decrease in peak intensity and loss of crystal peaks around the 2θ area at 9, 13, 25, 27, and 71. These XRD results also show the influence of swelling agents that influence the formation of single phases[35]. From the results of the XRD, the crystals derived from ZAL are triclinic form with a crystal density of 3.361 g/cm³, while the ZAL Swelling shows an orthorhombic crystal form with a crystal density of 2.062 g/cm³.

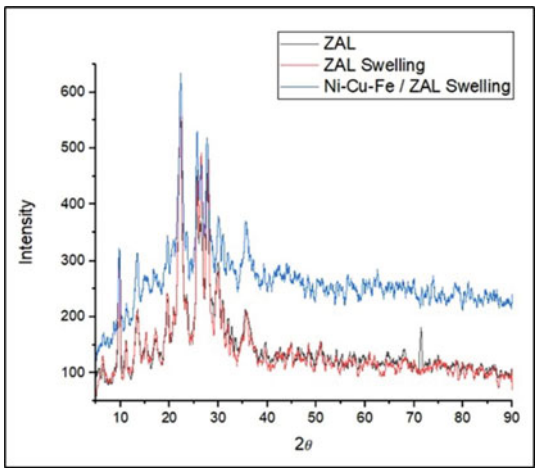

Figure 2. XRD Spectra Profile of ZAL; ZAL Swelling; and Cu-Ni-Fe/ZAL Swelling Catalysts

XRD results of Cu-Ni-Fe/ZAL Swelling show the fraction peaks reflected at 2θ = 9.82, 13.08, 25.66, 26.36, 27.42, 27.52, 27.6, 30.32, 36.42 for Cu-Ni-Fe/ZAL Swelling. In comparison, ZAL Swelling diffraction peaks reflected at 2θ = 9.74, 13.33, 17.29, 19.76, 22.32, 25.63, 26.32, 26.60, 27.66, 28.01, 29.99, 35.84. The overall trend intensity shows an increase in crystal growth from 100%, and the condition of the increase in trend intensity shows the addition of new crystals derived from the addition of Cu-Ni-Fe metal. In Cu-Ni-Fe/ZAL Swelling, there is a significant increase in peak intensity of 18% and 50% at 2θ in areas 22 and 35, respectively. In addition, there is a decrease in peak intensity in the addition of Cu-Ni-Fe metal seen at 2θ in areas 27 and 30, and this shows a decrease in the quality of Si and Al around these areas. The decrease in peak intensity shows the influence of acid originating from Cu-Ni-Fe which is an acidic metal

that results in a change in the zeolite structure into a single-phase form[35–37]. The peak analysis shows that the crystal structure of SiO_2 is tetrahedral while AlO_2 is cubic. These XRD results indicate a change in crystal form from orthorhombic with a crystal density of 2.289 gr/cm^3 to triclinic combined with tetragonal for Cu-Ni-Fe/Zeolite swelling with a crystal density of 2.167 gr/cm^3.

SEM-EDX-Mapping Analysis

The SEM EDX results in Table 1 show a decrease in the mass % of the atomic elements of ZAL Swelling compared to ZAL, where a high decrease occurs in the atoms of Al, Na, and Ca, which are 43%, 40%, and 61%, respectively. This decrease is due to the reaction between the swelling agent $C_{15}H_{32}$ with alkali and alkaline earth metals through substitution and addition reactions. The change in the Si/Al ratio in ZAL Swelling has decreased by 10% compared to ZAL which has a Si/Al ratio of 5.9. This not-too-significant decrease in the Si/Al ratio shows that the structure and crystallinity of ZAL Swelling are maintained.

Table 1. EDX Analysis Results

Element	% Mass		
	ZAL	ZAL Swelling	Cu-Ni-Fe/ZAL Swelling
Na	3.45	3.60	0.00
Mg	0.89	1.14	0.80
Al	11.82	12.95	5.05
Si	69.50	68.09	54.61
K	4.34	5.31	3.65
Ca	3.79	3.91	0.97
Fe	3.04	2.24	9.44
Cu	3.18	2.77	14.12
Ni	0	0	11.36

In the Cu-Ni-Fe/ZAL Swelling catalyst, the most significant mass % increase occurred in Cu and Fe atoms, which increased by 68.5% and 54.9%, respectively. Meanwhile, atoms such as Ni, previously not present in ZAL Swelling, are now present at 3.98% by mass. For Si, Mg, and K atoms, the mass % increased by 23.4%, 7.6%, and 5.7%. These results show that adding a strongly acidic Cu-Ni-Fe metal solution can significantly remove Na metal and reduce Ca metal[38, 39]. These two metals are from the alkali and alkaline earth groups except for Mg and K, which experienced a not too-significant increase, or it can be said that no reaction occurred. The Si/Al ratio results also experienced a significant increase of 10.8 from the previous 5.9 caused by adding acidic Cu, Ni, and Fe metal solutions[40, 41].

The SEM and Mapping results in Fig. 3(a) and Fig. 3(b) show a drastic change in morphology, where the ZAL Swelling produces clumps with a larger diameter and a smoother surface than ZAL. Mapping results in Fig. 4(a) and Fig. 4(b) also provide a clearer picture of Si atoms than in ZAL. The addition of Cu-Ni-Fe metal to ZAL Swelling, where the catalyst Cu-Ni-Fe/ZAL Swelling decreased crystallinity, is evidenced by the reduction of carbon atom compounds (C) by 32%. The outer layer of Cu-Ni-Fe/ZAL Swelling based on SEM results Fig. 3(c) shows an uneven surface and appears to have a layer. This condition shows that Cu-Ni-Fe metal has entered the cage and channel structure of zeolite, replacing the position of Ca, Na, and extra framework atoms and the framework of Al[8, 42].

The surface is dominated by Si atoms, which are evenly distributed throughout the surface of ZAL Swelling. SEM Mapping Results Figure 4(c) shows that overall the Cu--Ni-Fe atoms are evenly distributed and some parts look brighter. This shows the dominance of Ni and Fe atoms bound to Cu atoms. most of the others are dominated by blue which is the Fe atom at the top while Ni and Cu are in the next layer. This position is because Fe is more insoluble than Ni and Cu.

BET Analysis

Brunauer, Emmett, and Teller (BET) analysis using NH_3 gas in Table 2, ZAL Swelling experienced an increase in average pore radius of 36% compared to ZAL, which was only 70.66 Å. In addition, there was a decrease in total pore volume by 2% and an increase in pore radius from 15.27 Å to 19.12 Å in ZAL swelling. These results indicate that ZAL has generally experienced swelling due to interaction with the swelling agent. The use of Swelling agent $C_{15}H_{32}$ consisting of aromatic structure and open chain can provide swelling influence accompanied by removal of alkali and alkaline earth metals[43, 44, 45, 46, 47].

ZAL Swelling that has been encapsulated Cu-Ni-Fe metal (Cu-Ni-Fe/ZAL Swelling) The results of Table 2 show an increase in the value of total pore volume but a decrease in average pore radius. This change is due to some space in ZAL Swelling being successfully filled by metal, or the metal is encapsulated in the pore and volume of zeolite[48]. These results also show that the addition or increase in volume leads vertically, causing a narrowing of the pore radius. In addition, the acidic nature of Cu-Ni-Fe metal allows it to break the Al bond[39, 49]. This is evidenced by the increase in total pore volume and surface area compared to SEM-EDX data.

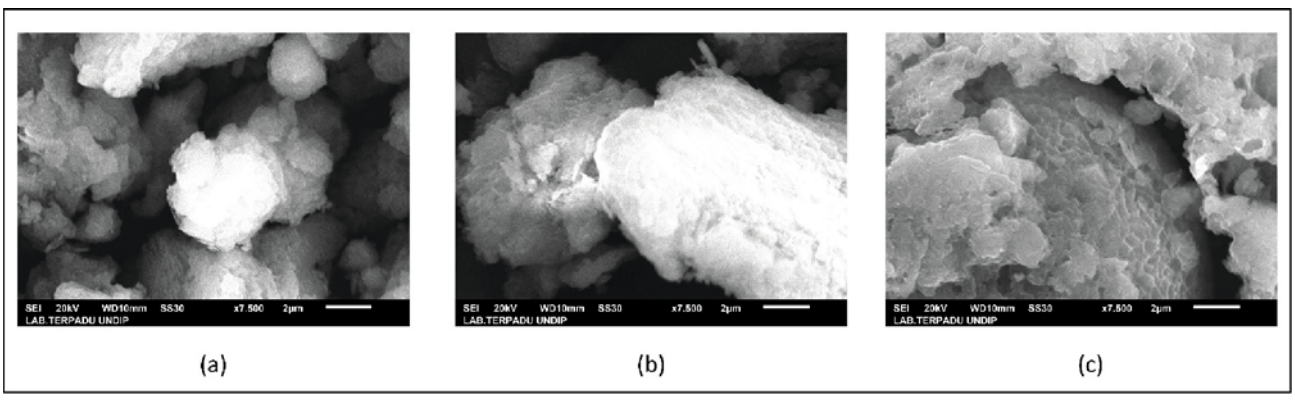

Figure 3. SEM profile of (a) ZAL, (b) ZAL Swelling, (c) Cu-Ni-Fe/ZAL Swelling

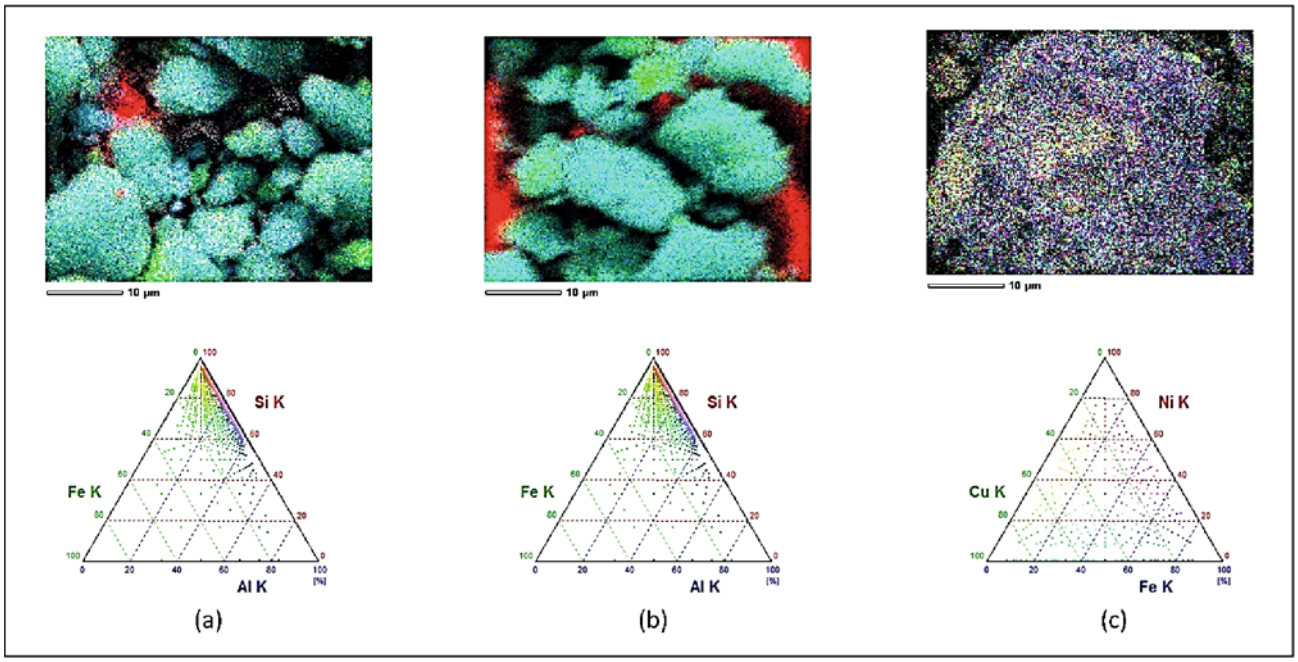

Figure 4. SEM Profile Mapping (a) ZAL, (b) ZAL Swelling, (c) Cu-Ni-Fe/ZAL Swelling

Figure 5 is a curve of the size distribution of pore radii using nitrogen adsorption where the y-axis shows the size distribution of pore radii while the x-axis is the pore radius. From the profile in Figure 5, it shows that the size of the pores is not uniform. Where the distribution of pore radius sizes of 20 to 60 Å (mesopores) for ZAL Swelling is 54.54% while Cu-Ni-Fe/ZAL Swelling is 70%. This indicates that Cu-Ni-Fe/ZAL Swelling is more mesoporous than ZAL Swelling (Leong et al. 2018; Shiraishi 2003;[28].

The isotherm graphs of adsorption-desorption results of N_2 gas Fig. 6, from Cu-Ni-Fe/ZAL Swelling, are included in the type IV classification, where it has a multilayered layer or multilayer[52]. This result can be compared with the spectra mapping produced by Cu-Ni-Fe/ZAL Swelling, where there is color degradation on the surface of the zeolite.

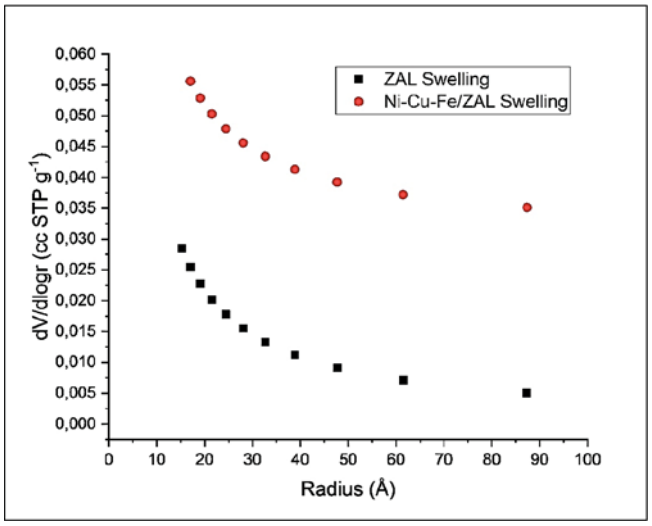

Figure 5. Size Distribution of Pore Radius of Cu-Ni-Fe/ZAL Swelling

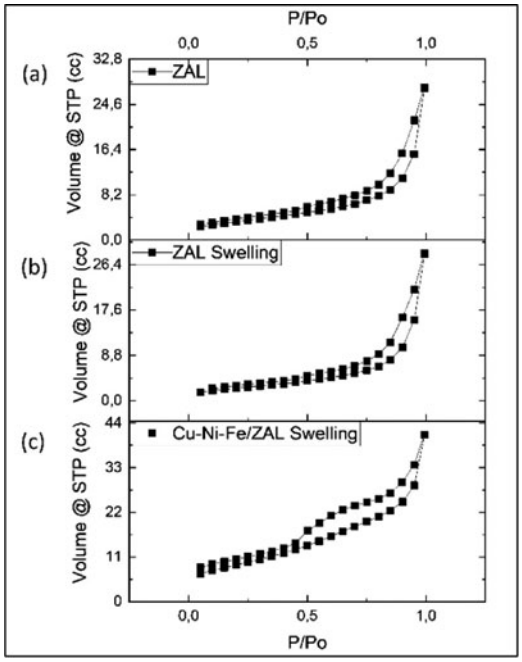

Figure 6. Low-temperature Nitrogen Adsorption Isotherm of (a) ZAL, (b) ZAL Swelling, (3) Cu-Ni-Fe/ZAL Swelling Catalysts

Weight Loss Analysis

The TGA test results on ZAL and ZAL Swelling in Figure 7(a) show the relationship between temperature changes and weight loss. At temperatures of 100–130 °C, there is a partial loss of water content, where ZAL and ZAL Swelling experience weight loss of 5.69% and 4.76%, respectively. The decrease or % weight loss continues

Table 2. Texture Properties of ZAL, ZAL Swelling, Cu-Ni-Fe/ZAL Catalyst Swelling

1	Total pore volume (cc/g)	Average pore radius (Å)	BJH Pore Size Distribution Adsorption Data		
			Surface Area	Pore Volume	Pore Radius Dv(r)
ZAL	0.102	70.66	19.64 m²/g	0.097 cc/g	15.27 Å
ZAL Swelling	0.097	95.84	17,07 m²/g	0.095 cc/g	19.12 Å
Cu-Ni-Fe/ZAL Swelling	0.101	39.51	29,74 m²/g	0.087 cc/g	17.04 Å

until the temperature is 540 °C. The weight loss in ZAL Swelling looks more stable than in ZAL, and this condition is influenced by the average pore radius of 35.64% larger, the total pore volume, which is 5.55% smaller than ZAL shows an increase in mesoporosity, and a higher Si/Al ratio[53–55].

The weight loss profile in Fig. 7(b) shows that from 250 °C to 130 °C, water molecules are removed in ZAL Swelling and Cu-Ni-Fe/ZAL Swelling. This is characterized by a weight loss of 5.71% and 5.95% for ZAL and Cu-Ni-Fe/ZAL Swelling. Removal of bound water molecules and impurity compounds continues up to a temperature of 375 °C. At this temperature, the same weight loss of 8.89% was observed for ZAL Swelling and Cu-Ni-Fe/ZAL Swelling.

At temperatures above 375 °C to 490 °C, the decrease in weight loss Cu-Ni-Fe/ZAL Swelling is smaller than that of ZAL Swelling. Cu-Ni-Fe/ZAL Swelling slightly formed hydroxyl bonds of water molecules. This condition is indicated by an increase in the Si/Al ratio, where ZAL Swelling is 5.3 while Cu-Ni-Fe/ZAL Swelling is 10.81, which influences thermal stability[54, 55]. The increase in Cu-Ni-Fe cations in Cu-Ni-Fe/ZAL Swelling pores provides better thermal stability resistance characterized by a % weight loss of only 0.86% at 375–490 °C[55].

Acidity Profile Analysis

The acid distribution profile of ZAL and ZAL Swelling from the TPD spectra results in Fig. 8(a) low range temperature, which is the Lewis acid area (100–550 °C), showing the peak area of ZAL Swelling (200–230 °C) is slightly higher than the peak area produced by ZAL. Meanwhile, in the Bronsted acid sites area (650–750 °C), the peak area of ZAL is higher. This indicates that ZAL Swelling has a higher Bronsted acid strength than ZAL.

The increase in Bronsted acid sites is inseparable from the loss of some alkali and alkaline earth metals that are more like Lewis acids[56]. his result is also comparable

Table 3. Total Acid Strength

No.	Sample	Acidity (mmol/gr)
1	ZAL	2.0106
2	ZAL Swelling	2.0443
3	Cu-Ni-Fe/ZAL Swelling	2.2595

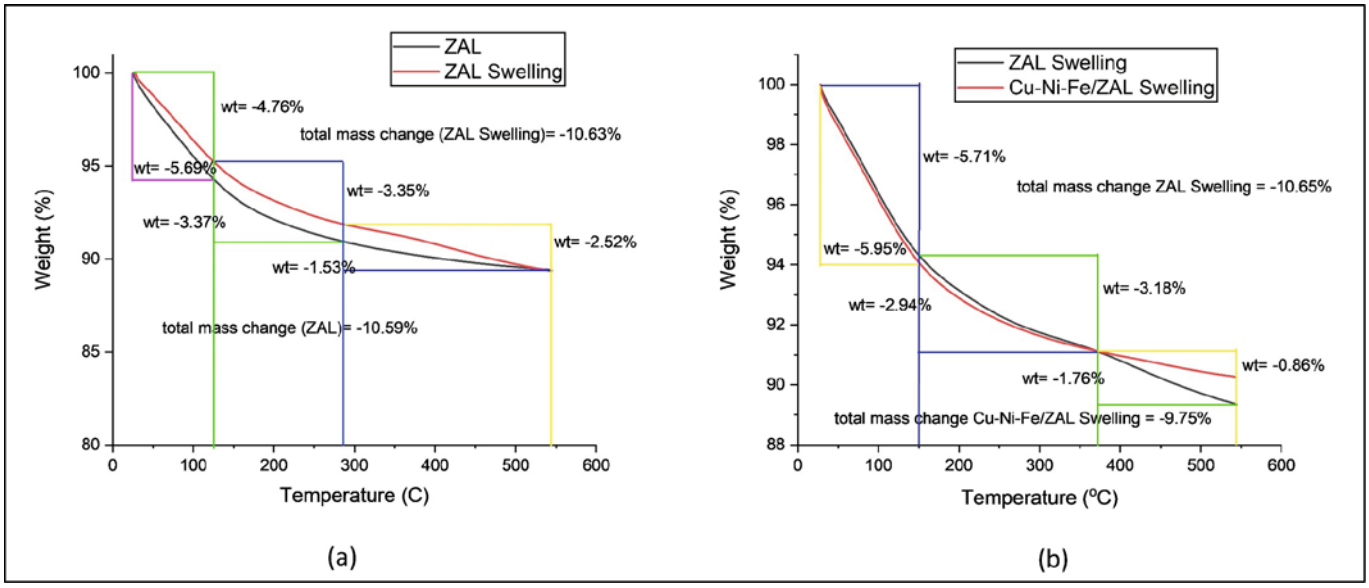

Figure 7. Weight Loss Profiles

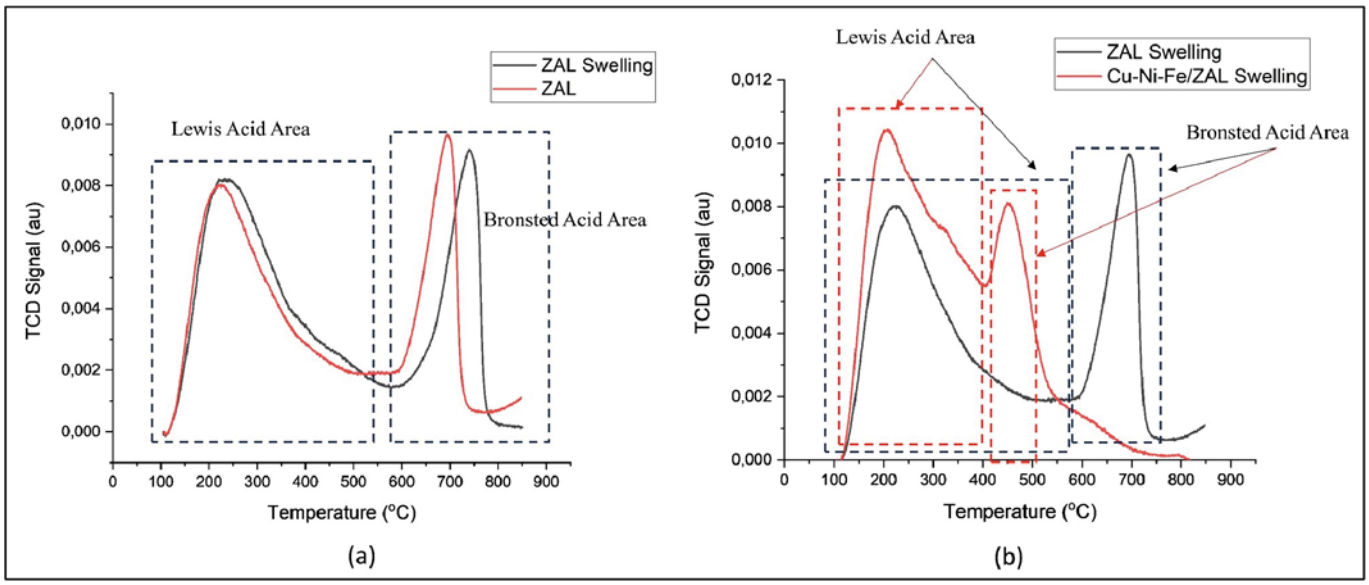

Figure 8. NH_3-TPD profiles of ZAL, ZAL Swelling, and Cu-Ni-Fe/ZAL Swelling

to the data displayed in the SEM EDX FTIR results, where some alkali and alkaline earth metals such as Na, Al, Ca, Mg, and Fe have decreased mass % in ZAL Swelling. The decrease in Si/Al ratio in ZAL Swelling compared to ZAL by 9.71% did not have a significant effect on the decrease of Bronsted acid sites.

The addition of Cu-Ni-Fe metals to ZAL Swelling based on TPD spectra data Fig. 8(b) shows the acid distribution profile of ZAL Swelling and Cu-Ni-Fe/ZAL Swelling for each temperature change. From the measurement chart above, there are 2 peaks, namely at low temperature which shows weak acid and high temperature which shows strong acid[57, 58, 59]. Weak acid which is a Lewis acid both ZAL Swelling and Cu-Ni-Fe/ZAL Swelling is in the temperature range of 190–220 °C, while strong acid which is the area of Brønsted acid is for Cu-Ni-Fe/ZAL Swelling is at a temperature of 440–460 °C while in ZAL Swelling is at 690–710 °C. The results of TPD spectra low range temperature show the peak area of Cu-Ni-Fe/ZAL Swelling is much higher than the peak area produced by ZAL Swelling providing information that Cu, Ni, and Fe metals can increase the strength of Lewis acid[60]. The strength of the distribution of Lewis acid sites owned by Cu-Ni-Fe/ZAL Swelling is slightly more even than the Lewis acid sites owned by ZAL Swelling[60]. In this situation, the strength of the acid distribution is closely related to the acid strength of the Lewis acid site distribution.

In the strong acid or Brønsted acid area, Cu-Ni-Fe/ZAL Swelling (100–400 °C) has a lower peak area temperature than the peak area temperature owned by ZAL Swelling. This indicates that the distribution of Brønsted acid sites owned by Cu-Ni-Fe/ZAL Swelling is much more even[60]. The condition of the distribution of Lewis acid sites and Brønsted acid of Cu-Ni-Fe/ZAL Swelling is comparable to the SEM EDX Mapping results, which show an even distribution of Cu-Ni-Fe metal. The peak area of Cu-Ni-Fe/ZAL Swelling is lower than that of ZAL Swelling, and this result shows that adding Cu-Ni-Fe metal can regulate the acid strength of both Lewis acid and Brønsted acid from ZAL Swelling[60]. Overall, the resulting TCD spectra profile of Cu-Ni-Fe/ZAL Swelling illustrates that the temperature area that should be the Lewis acid site area of ZAL Swelling (100–550 K), now has 2 profiles of both Lewis acid site and Bronsted acid site. The presence of 2 acidic area profiles of the Cu-Ni-Fe/ZAL Swelling catalyst in the temperature range of 100-550 K indicates this catalyst is amphoteric. The NH3-TPD profile resulting from the Cu-Ni-Fe/ZAL Swelling catalyst provides optimization of Lewis and Brønsted acid areas exhibiting amphoteric properties[61].

The removal and reduction of several types of metals that are strong bases such as Na, Mg, K, and Ca have an impact on reducing alkaline properties. While reducing the content of Si tends to limit the strong acid or Brønsted acid of ZAL. Cu, Ni, and Fe metals, which are periodically weakly alkaline, tend to affect the increase of Lewis acid.

CONCLUSION

The change of ZAL structure to ZAL Swelling influenced the increase of average pore radius in ZAL Swelling by 36% and was accompanied by the reduction of Al, Na, and Ca atoms by 43%, 40%, and 61%, respectively, compared to ZAL. In addition to producing an extensive framework, this ZAL Swelling structure increases acid strength and better distributes Bronsted acid sites than Lewis acid sites. Adding Cu, Ni, and Fe metals to ZAL Swelling, which produces Cu-Ni-Fe/ZAL Swelling catalyst, has higher acidity properties of Lewis acid sites and a more even distribution than Bronsted acid sites. This proves that the addition of Cu, Ni, and Fe metals can regulate the acidic strength of ZAL Swelling. Besides, the TCD Spectra profile testing using the NH_3-TPD method shows that the temperature area of Lewis acid sites and Brønsted acid sites of the catalyst Cu-Ni-Fe/ZAL Swelling is in the area of Lewis acid sites on ZAL Swelling. This indicates that the Cu-Ni-Fe/ZAL Swelling catalyst is amphoteric.

LITERATURE CITED

1. Minceva, M., Fajgar, R., Markovska, L., Meshko, V. (2008). Comparative Study of Zn2+, Cd2+, and Pb2+ Removal From Water Solution Using Natural Clinoptilolitic Zeolite and Commercial Granulated Activated Carbon. Equilibrium of Adsorption. *Separ. Sci. Technol. Pap.* 43(8), 2117–43. DOI: 10.1080/01496390801941174.

2. Król, M. (2020). Natural vs. Synthetic Zeolites. Crystals. DOI: 10.3390/cryst10070622.

3. Muzwar, K., Hidajat, W., Winarno, T. (2018). Genesis dan Karakteristik Endapan Zeolit Desa Hargomulyo dan Sekitarnya, Kecamatan Gedangsari, Gunung Kidul, Daerah Istimewa Yogyakarta. *J. Geosains Dan Teknologi. Pap*. 1, 19. DOI: 10.14710/jgt.1.1.2018.19-24.

4. Razzak, M., Las, T., Priyambodo, P. (2013). The Characterization of Indonesian's Natural Zeolite For Water Filtration System. *J. Kimia VALENSI. Pap*. 3. DOI: 10.15408/jkv.v3i2.518.

5. Syafriadi., Marhamah, S., Al Muttaqii, M. (2021). PENGARUH VARIASI KONSENTRASI NaOH PADA ZEOLIT ALAM LAMPUNG TERHADAP PRODUK SILIKA. *J. Riset Teknologi Ind. Pap*. 15, 393–402.

6. Khivantsev, K., Gramatikov, S., Jaegers, N., Derewinski, M., Vayssilov, G., Szanyi, J., Aleksandrov, H. (2022). Direct observation of a new aluminum Lewis acid site in a zeolite.

7. Johnson, B., Iorio, J., Roman-Leshkov, Y. (2021). Identification and quantification of distinct active sites in Hf-Beta zeolites for transfer hydrogenation catalysis. *J. Catalysis. Pap.* 404. DOI: 10.1016/j.jcat.2021.10.026.

8. Ates, A. (2019). The modification of aluminium content of natural zeolites with different composition. *Powder Technol. Pap*. 344. DOI: 10.1016/j.powtec.2018.12.018.

9. Lusardi, M., Davis, M. (2019). Investigation of the active Bronsted acid site for the DME carbonylation reaction in chabazite-type zeolites.

10. Kong, H.-Y., Chen, H.-D., Yu, R., Zhang, W.-P. (2021). A Combination of DFT and Solid-state NMR Study on the Relationship between Framework Al Distribution and Bronsted Acidity in SSZ-39 Zeolite. *J. Molec. Catal. Pap*. 35, 215–25. DOI: 10.16084/j.issn1001-3555.2021.03.002.

11. Zhang, L., Ma, X., Zheng, J., Liu, Y., Qin, B., Du, Y. (2022). Active Zn Species Nest in Dealumination Zeolite Composite for Propane Dehydrogenation. Catal. Letters. DOI: 10.1007/s10562-022-04244-4.

12. Sasongko, S., Anggoro, D.D., Buchori, L., Febrianto, R., Siagian, E. (2020). The effect of dealumination process on zeolite Y acidity and morphology. vol. 2197.

13. Wang, S., He, Y., Jiao, W., Wang, J., Fan, W. (2019). Recent experimental and theoretical studies on Al siting/acid

site distribution in zeolite framework. *Current Opinion Chem. Engin.* DOI: 10.1016/j.coche.2019.04.002.

14. Palčić, A., Valtchev, V. (2020). Analysis and control of acid sites in zeolites. *Appl. Catal. A: General*. DOI: 10.1016/j.apcata.2020.117795.

15. Boronat, M., Corma, A. (2015). Factors Controlling the Acidity of Zeolites. *Catal. Letters. Pap.* 145(1), 162–72. DOI: 10.1007/s10562-014-1438-7.

16. Mondal, P., Hazarika, K.K., Deka, A., Deka, R.C. (2008). Density functional studies on Lewis acidity of alkaline earth metal exchanged faujasite zeolite. Molec. Simulation. Pap. 34(10–15), 1121–8. DOI: 10.1080/08927020802073032.

17. Huang, M., Kaliaguine, S. (1992). Lewis acid and Lewis basic Sites in Alkali-exchanged Zeolites - characterization and catalytic activity. In: Smith, K.J., Sanford, E.C.B.T.-S. in S.S. and C., editors. Progress in Catalysis, vol. 73. Elsevier p. 291–300.

18. Chalupka, K., Sadek, R., Valentin, L., Millot, Y., Calers, C., Nowosielska, M., Rynkowski, J., Dzwigaj, S. (2018). Dealuminated Beta Zeolite Modified by Alkaline Earth Metals. *J. Chem. Pap.* 2018, 7071524. DOI: 10.1155/2018/7071524.

19. Li, X., Dong, W., Zhang, J., Shao, S., Cai, Y. (2020). Preparation of bio-oil derived from catalytic upgrading of biomass vacuum pyrolysis vapor over metal-loaded HZSM-5 zeolites. *J. Energy Instit. Pap*. 93(2). DOI: 10.1016/j.joei.2019.06.005.

20. Zhang, R., Zou, R., Li, W., Chang, Y., Fan, X. (2022). On understanding the sequential post-synthetic microwave--assisted dealumination and alkaline treatment of Y zeolite. *Microp. Mesop. Mater. Pap.* 333, 111736. DOI: 10.1016/j.micromeso.2022.111736.

21. Yang, F., Fu, J., Mo, J., Xiuyang, L. (2013). Synergy of Lewis and Brønsted Acids on Catalytic Hydrothermal Decomposition of Hexose to Levulinic Acid. *Energy & Fuels. Pap.* 27, 6973–6978. DOI: 10.1021/ef401560v.

22. Songtawee, S., Rungtaweevoranit, B., Klaysom, C., Faungnawakij, K. (2021). Tuning Brønsted and Lewis acidity on phosphated titanium dioxides for efficient conversion of glucose to 5-hydroxymethylfurfural. *RSC Advances. Pap*. 11(47), 29196–206. DOI: 10.1039/D1RA06002C.

23. Vosmerikova, L.N., Matieva, Z.M., Snatenkova, Y.M., Kolesnichenko, N.V., Zaikovskii, V.I., Vosmerikov, A.V. (2022). Conversion of dimethyl ether to liquid hydrocarbons over Zn--isomorphously substituted HZSM-5. *Fuel. Pap.* 320, 123959. DOI: 10.1016/J.FUEL.2022.123959.

24. Liu, M., Jia, S., Li, C., Zhang, A., Song, C., Guo, X. (2014). Facile preparation of Sn-β zeolites by post-synthesis (isomorphous substitution) method for isomerization of glucose to fructose. *Chin. J. Catal. Pap.* 35(5), 723–32. DOI: 10.1016/S1872-2067(14)60071-1.

25. Yue, Q., Zhang, J., Shamzhy, M., Opanasenko, M. (2019). Seeded growth of isomorphously substituted chabazites in proton-form. *Microp. Mesop. Mater. Pap*. 280, 331–6. DOI: 10.1016/J.MICROMESO.2019.02.017.

26. Gackowski, M., Datka, J. (2020). Acid properties of hierarchical zeolites Y. *Molecules*. DOI: 10.3390/molecules25051044.

27. Zheng, Y., Li, D., Wang, J., Lyu, B., Long, B., Ding, Z., Zheng, Z. (2021). Production of bio-aromatic by catalytic biomass pyrolysis over metal modified biomass-derived biochar--based catalyst. Nongye Gongcheng Xuebao/Transactions of the *Chinese Soc. Agric. Engin. Pap.* 37(5), 231–40. DOI: 10.11975/j.issn.1002-6819.2021.05.027.

28. Darmansyah, D., Ginting, S., Iryani, D., Sari, R., Supriyadi, D. (2021). Characterization of Modified Lampung Natural Zeolite with Cetyl Trimethyl Ammonium Bromide (CTAB) for Adsorption Industrial Tapioca Wastewater.

29. Ginting, S., Yulia, Y., Wardono, H., Darmansyah, D., Hanif, M., Iryani, D. (2019). Synthesis and Characterization of Zeolite Lynde Type A (LTA): Effect of Aging Time. J. Physics: Conf. Series. Pap. 1376, 12041. DOI: 10.1088/1742-6596/1376/1/012041.

30. Sáez Del Bosque, I.F., Martínez-Ramírez, S., Blanco--Varela, M.T. (2014). FTIR study of the effect of temperature and nanosilica on the nano structure of C–S–H gel formed by hydrating tricalcium silicate. *Constr. Building Mater. Pap.* 52, 314–23. DOI: 10.1016/J.CONBUILDMAT.2013.10.056.

31. Xu, S., Wang, Q., Wang, N., Song, Q., Li, Y. (2022). Effects of natural zeolite replacement on the properties of superhydrophobic mortar. *Constr. Building Mater. Pap*. 348, 128567. DOI: 10.1016/J.CONBUILDMAT.2022.128567.

32. Al-Oweini, R., El-Rassy, H. (2009). Synthesis and characterization by FTIR spectroscopy of silica aerogels prepared using several Si(OR)4 and R′′Si(OR′)3 precursors. *J. Molec. Struct. Pap*. 919(1–3), 140–5. DOI: 10.1016/J.MOLSTRUC.2008.08.025.

33. Król, M., Jeleń, P. (2021). The Effect of Heat Treatment on the Structure of Zeolite A. Mater. Pap. 14, 4642. DOI: 10.3390/ma14164642.

34. Ellerbrock, R., Stein, M., Schaller, J. (2022). Comparing amorphous silica, short-range-ordered silicates and silicic acid species by FTIR. *Sci. Reports. Pap.* 12(1), 11708. DOI: 10.1038/s41598-022-15882-4.

35. Ke, G., Shen, H., Yang, P. (2019). Synthesis of X-Zeolite from Waste Basalt Powder and its Influencing Factors and Synthesis Mechanism. *Materials.* DOI: 10.3390/ma12233895.

36. Elaiopoulos, K., Perraki, T., Grigoropoulou, E. (2010). Monitoring the effect of hydrothermal treatments on the structure of a natural zeolite through a combined XRD, FTIR, XRF, SEM and N2-porosimetry analysis. *Microp. Mesop. Mater. Pap.* 134(1–3), 29–43. DOI: 10.1016/J.MICROMESO.2010.05.004.

37. Ünveren, E., Gündüz, G., Cakicioğlu–Özkan, F. (2005). Isomerization of Alpha-pinene Over Acid Treated Natural Zeolite. *Chem. Engin. Commun. Pap*. 192(3), 386–404. DOI: 10.1080/00986440590477773.

38. Ates, A., Hardacre, C. (2012). The effect of various treatment conditions on natural zeolites: Ion exchange, acidic, thermal and steam treatments. *J. Colloid Interf. Sci. Pap*. 372(1), 130–40. DOI: 10.1016/J.JCIS.2012.01.017.

39. Beyer, H. (2002). Dealumination Techniques for Zeolites. Mol. Sieves, Pap. 3, 203–55.

40. Wang, C., Leng, S., Guo, H., Yu, J., Li, W., Cao, L., Huang, J. (2019). Quantitative arrangement of Si/Al ratio of natural zeolite using acid treatment. *Appl. Surf. Sci. Pap*. 498, 143874. DOI: 10.1016/J.APSUSC.2019.143874.

41. Burris, L.E., Juenger, M.C.G. (2016). The effect of acid treatment on the reactivity of natural zeolites used as supplementary cementitious materials. *Cement Conc. Res. Pap*. 79, 185–93. DOI: 10.1016/J.CEMCONRES.2015.08.007.

42. Tang, G., Li, Y., Wang, Y., Chai, Y., Liu, C. (2022). A review on the synthesis, structural modification and application of two-dimensional MFI zeolite. *J. Porous Mater. Pap*. 29(6), 1649–66. DOI: 10.1007/s10934-022-01304-3.

43. Bruckner, R., Harmata, M. (2010). Substitution Reactions on Aromatic Compounds BT - Organic Mechanisms: Reactions, Stereochemistry and Synthesis. Berlin, Heidelberg: Springer Berlin Heidelberg p. 201–57.

44. O'Neill, M.E., Wade, K. (1982). 1 - Structural and Bonding Relationships among Main Group Organometallic Compounds. In: Wilkinson, G., Stone, F.G.A., Abel, E.W.B.T.-C.O.C., editors. Oxford: Pergamon p. 1–42.

45. Chen, R., Li, L. (2001). Reactions of atomic transition--metal ions with long-chain alkanes. *J. Amer. Soc. Mass Spectrom. Pap.* 12(4), 367–75. DOI: 10.1016/S1044-0305(01)00217-3.

46. Armentrout, P.B., Beauchamp, J.L. (1989). The chemistry of atomic transition-metal ions: insight into fundamental aspects of organometallic chemistry. Accounts of Chemical Research. Pap. 22(9), 315–21. DOI: 10.1021/ar00165a004.

47. Jørgensen, K.A. (1991). A Review of: "Bonding Energetics in Organometallic Compounds. Edited by Tobin J. Marks. ACS Symposium Series No. 428, American Chemical Society, Washington, DC, 1990, xi + 305pp., $ 64.95. ISBN

0-8412-1791-2." Sulfur Reports. Pap. 11(1) 201–2. DOI: 10.1080/01961779108048769.

48. Shui, H., Xu, H., Zhou, Y., Shui, T., Pan, C., Wang, Z. (2017). Study on hydro-liquefaction kinetics of thermal dissolution soluble fraction from Shenfu sub-bituminous coal. *Fuel. Pap.* 200, 576–82. DOI: 10.1016/J.FUEL.2017.03.048.

49. Yoshioka, T., Iyoki, K., Hotta, Y., Kamimura, Y., Yamada, H., Han, Q. (2023). Dealumination of small-pore zeolites through pore-opening migration process with the aid of pore-filler stabilization. *Sci. Adv. Pap.* 8(25) eabo3093. DOI: 10.1126/sciadv.abo3093.

50. Shiraishi, S. (2003). Electric Double Layer Capacitors. Carbon Alloys: Novel Concepts to Develop Carbon Science and Technology. Pap. 447–57. DOI: 10.1016/B978-008044163-4/50027-9.

51. Leong, J., Seo, Y., Chu, S.-H., Park, C., Jeon, E.J., Cho, S.-W. (2018). Pore Diameter of Mesoporous Silica Modulates Oxidation of H2O2-Sensing Chromophore in a Porous Matrix. *Langmuir. Pap*. 34(38), 11242–11252. DOI: 10.1021/acs.langmuir.8b00957.

52. Al-Ghouti, M.A., Da'ana, D.A. (2020). Guidelines for the use and interpretation of adsorption isotherm models: A review. *J. Hazard. Mater. Pap.* 393, 122383. DOI: 10.1016/J.JHAZMAT.2020.122383.

53. Musyoka, N.M., Petrik, L.F., Hums, E., Kuhnt, A., Schwieger, W. (2015). Thermal stability studies of zeolites A and X synthesized from South African coal fly ash. *Res. Chem. Intermed. Pap.* 41(2), 575–82. DOI: 10.1007/s11164-013-1211-3.

54. Usachev, N., Belanova, E., Krukovsky, I., Kanaev, S., Atal"yan, O., Kazakov, A. (2003). Thermal transformations in systems based on zeolites Y, X, and A containing zinc and sodium nitrates. Russian Chemical Bulletin - RUSS CHEM BULL. Pap. 52, 1940–9. DOI: 10.1023/B:RUCB.0000009636.89718.56.

55. Cruciani, G. (2006). Zeolites upon heating: Factors governing their thermal stability and structural changes. *J. Phys. Chem. Solids. Pap.* 67(9–10), 1973–94. DOI: 10.1016/J.JPCS.2006.05.057.

56. Fermoso, J., Hernando, H., Jana, P., Moreno, I., Přech, J., Ochoa-Hernández, C. (2016). Lamellar and pillared ZSM-5 zeolites modified with MgO and ZnO for catalytic fast-pyrolysis of eucalyptus woodchips. *Catal. Today. Pap.* 277, 171–81. DOI: 10.1016/j.cattod.2015.12.009.

57. Chen, H., Wang, M., Yang, M., Shang, W., Yang, C., Liu, B., Hao, Q., Zhang, J., Ma, X. (2019). Organosilane surfactant-directed synthesis of nanosheet-assembled SAPO-34 zeolites with improved MTO catalytic performance. *J. Mater. Sci. Pap.* 54. DOI: 10.1007/s10853-019-03485-w.

58. Ma, T., Imai, H., Yamawaki, M., Terasaka, K., Li, X. (2014). Selective Synthesis of Gasoline-Ranged Hydrocarbons from Syngas over Hybrid Catalyst Consisting of Metal-Loaded ZSM-5 Coupled with Copper-Zinc Oxide. *Catal. Pap.* 4, 116–28. DOI: 10.3390/catal4020116.

59. Dugkhuntod, P., Imyen, T., Wannapakdee, W., Yutthalekha, T., Salakhum, S., Wattanakit, C. (2019). Synthesis of hierarchical ZSM-12 nanolayers for levulinic acid esterification with ethanol to ethyl levulinate. *RSC Advances*. Pap. 9, 18087–97. DOI: 10.1039/C9RA03213D.

60. Damjanović, L., Auroux, A. (2009). Determination of Acid/Base Properties by Temperature Programmed Desorption (TPD) and Adsorption Calorimetry BT – Zeolite Characterization and Catalysis: A Tutorial. In: Chester, A.W., Derouane, E.G., editors. Dordrecht: Springer Netherlands Pap. 107–67.

61. Lilic, A., Wei, T., Bennici, S., Devaux, J.-F., Dubois, J.-L., Auroux, A. (2017). A Comparative Study of Basic, Amphoteric, and Acidic Catalysts in the Oxidative Coupling of Methanol and Ethanol for Acrolein Production. *ChemSusChem. Pap*. 10. DOI: 10.1002/cssc.201701040.